ADVANCED ENGINEERING MATERIALS
www.aem-journal.com

Mechanical Properties of Different Austenitic High-Nitrogen Steel Grades Produced by Powder Mixtures

Felix Radtke, Louis Becker, Lars Schultze-Schlutius, Anke Kaletsch, Jonathan Lentz, Sebastian Weber, and Christoph Broeckmann*

The advantages of nitrogen as an alloying element in austenitic stainless steels has been recognized for decades. However, its solubility varies across steel phases, with the highest in the austenitic solid state. Recent studies show that Si_3N_4 and X2CrNi18-9 (AISI 304L) powder mixtures enable solid-state alloy formation. During hot isostatic pressing (HIP), Si_3N_4 dissolves, allowing nitrogen diffusion into the austenitic matrix, forming high-nitrogen steel (HNS). This study examines the mechanical properties of HNS produced via powder metallurgy HIP and additive manufacturing using a shell-core scanning strategy, followed by HIP densification. Processing routes significantly affect microstructure and nitrogen content. Clear trends are found between hardness, tensile strength, and high-cycle fatigue strength, influenced by processing conditions and nitrogen levels. Additionally, Si_3N_4 particle size distribution impacts microstructure, with larger particles reducing grain size and enhancing strength. A linear relationship is observed between nitrogen content and both hardness and tensile strength.

1. Introduction

Nitrogen exhibits outstanding properties as an alloying element in austenitic stainless steels. Like carbon, it dissolves interstitially, stabilizes the austenite phase, and enhances strength due to solid solution strengthening. Due to its electron configuration, it is assumed that increasing strength does not result in reduced ductility—a phenomenon that is highly atypical and, therefore, of significant relevance for various applications for CrMn steel grades.[1] However, nitrogen's solubility in Fe-based materials poses a challenge. While nitrogen strongly stabilizes the face-centered cubic austenitic phase and exhibits high solubility in this structure, its solubility in the body-centered cubic ferritic phase or in the liquid phase is limited. This complicates the production and processing of high-nitrogen steels (HNS), where the aim is to achieve a maximum nitrogen content.[2–5]

The term HNS has been defined in various ways. Berns et al.[4] describe HNS as materials with "intentionally raised nitrogen content" achieved through alloying or powder metallurgy under pressure. Currently, the most common production method is pressurized electro-slag remelting (PESR), which exploits high-nitrogen partial pressure to dissolve nitrogen in the liquid phase, like the 1.4 108 stainless steel.[6] However, this approach has limitations, including high production costs and restrictions on semifinished product sizes. Consequently, research into alternative manufacturing methods for HNS components remains a priority.

Additive manufacturing (AM) is particularly appealing for producing small series of components with minimal material waste, making it an attractive method for highly alloyed materials.[7] Austenitic stainless steels, such as the Cr-Ni grade X2CrNiMo17-12-2 (AISI 316L),[8] dominate the literature on AM using powder bed fusion of metals using a laser beam (PBF-LB/M). Other alloys, for example AISI 304L,[9] AISI 318LN,[10] AISI H13,[11] or M2[12] have also been successfully processed through this method.

Developing HNS through powder metallurgy has seen significant progress. For example, large steel manufacturers like Georgsmarienhütte GmbH Germany, are producing HNS powders for powder-based process chains.[13] These efforts aim to retain a high-nitrogen content during atomization or to selectively adjust and increase nitrogen levels using advanced atomizing techniques. A study by Boes et al.[14] has shown that prealloyed nitrided X2CrNiMo17-12-2 powders ($N_{powder} = 0.273$ wt.-%) processed via PBF-LB/M suffer from high porosity (≈0.91%) and nitrogen losses of 20% ($N_{as\text{-}built} = 0.220$ wt.-%) during melting. Higher initial nitrogen content in powders correlates with increased losses in finished components, highlighting the challenge of nitrogen retention in the liquid phase.

F. Radtke, L. Schultze-Schlutius, A. Kaletsch, C. Broeckmann
Institute of Applied Powder Metallurgy and Ceramics at RWTH Aachen e. V.
RWTH Aachen University
520624 Aachen, Germany
E-mail: f.radtke@iwm.rwth-aachen.de

L. Becker, J. Lentz, S. Weber
Chair of Materials Technology
Ruhr-University Bochum
44801 Bochum, Germany

The ORCID identification number(s) for the author(s) of this article can be found under https://doi.org/10.1002/adem.202500885.

DOI: 10.1002/adem.202500885

A promising alternative involves in situ alloying using nitride additives during the PBF-LB/M process, bypassing the need for nitrogen enrichment during powder atomization. Valente et al.[15] demonstrated that Cr_2N addition to X2CrNiMo17-12-2 increased nitrogen content of up to 0.311 wt.-% in as-built components compared to base steel powders (0.098 wt.-%). However, high porosity and nitrogen losses persisted.

The use of powder mixtures appears to be the most promising approach, according to the literature. However, it is significantly limited by the solubility of the liquid phase. For this reason, it is advisable to take a step back and first focus on optimizing alloy formation before incorporating AM. In a work published recently, the authors of the present study introduced a novel approach to minimize nitrogen loss during liquid-phase processing and fully leverage nitrogen's high solubility in austenite.[16] This method enables the production of HNS from powder mixtures, using hot isostatic pressing (HIP). A mixture of X2CrNi18-9 powder and Si_3N_4 additives has been compacted, achieving a nearly interstitial distribution of nitrogen within the component with minimal nitrogen loss. **Figure 1** illustrates this approach, highlighting the effects of alloying elements (Si and N) and applied pressure on nitrogen solubility in austenite. However, challenges were observed, including an inhomogeneous distribution of silicon, and areas containing undissolved Si_3N_4 particles were identified.

Applying this concept to AM involves meeting two primary requirements: (1) ensuring undissolved Si_3N_4 particles remain in the component for subsequent diffusion alloying during HIP, and (2) achieving samples with a closed porosity for successful HIP densification. As with the dissolution behavior of Si_3N_4 particles, the particle size distribution (PSD) plays a crucial role in PBF-LB/M processing. Former studies[17] have shown that the addition of Si_3N_4 particles significantly worsens processability. Two particle size fractions have been identified as viable for processing. For the coarse fraction (36–71 µm), conventional mixing is sufficient to achieve acceptable powder properties. In contrast, the fine fraction (<36 µm) requires mechanical alloying using ball milling to ensure the powder properties are adequate for the PBF-LB/M process. Processing X2CrNi18-9 with Si_3N_4 particles via PBF-LB/M was identified as particularly challenging.[18] Achieving the combination of desired requirements (1) & (2) was not feasible. Si_3N_4 particles tended to favor the formation of pores and defects by uncontrolled Si_3N_4 dissolution, undermining the material's suitability for HIP postdensification. This led to the development of a new shell-core scanning strategy, aimed at separating properties into a gas-tight shell and a Si_3N_4 enriched core. Both the coarse Si_3N_4 fraction[19] and the fine fraction[20] demonstrated the effectiveness of this approach.

This study consolidates previously published processing strategies by systematically comparing the mechanical properties of components produced via HIP of loose powder (PM-HIP) and those fabricated using a combined process of laser-based powder bed fusion and hot isostatic pressing (AM-HIP). **Figure 2** illustrates the processing flowchart for two different fractions of Si_3N_4 particles that were utilized and blended with X2CrNi18-9 base powder using distinct mixing techniques. After mixing, the resulting powder blends were used both for conventional PM-HIP consolidation and for the AM-HIP route.

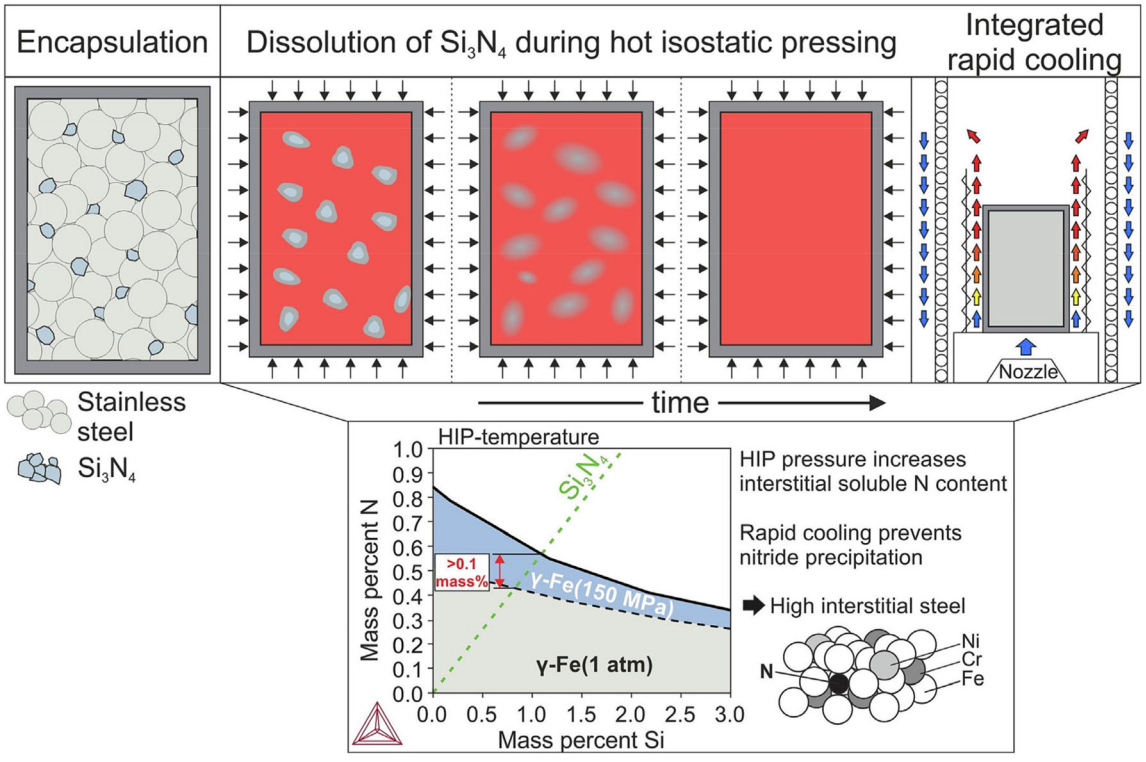

Figure 1. Demonstrating the process chain for PM-HIP production of high-nitrogen steels via a powder mixture containing Si_3N_4 as explained in a previous study.[16]

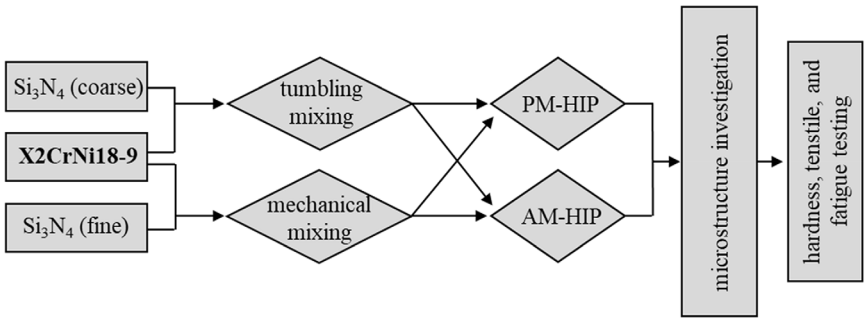

Figure 2. Flowchart to summarize the working plan of the manuscript.

The combination of varying PSDs, different mixing strategies, and distinct processing strategies exerts a significant influence on the resulting microstructure and final component properties. Therefore, the first part of this work investigates the microstructural evolution in terms of porosity, phase formation, grain size (GS), and nitrogen content. Subsequently, mechanical characterization comprising hardness, tensile, and fatigue testing is performed and correlated with the observed microstructural features. For comparison, a conventionally melted reference alloy (X2CrNiN18-9) with a nitrogen content of 0.12 wt% is also examined.

2. Experimental Section

2.1. Materials

2.1.1. Powders

The base material used in this work was the gas-atomized austenitic stainless steel powder X2CrNi18-9 (AISI 304L, DIN EN 1.4 307) produced by Carpenter Additive (Widnes, UK), in the particle size fraction of 20–50 µm. Si_3N_4 powder with particle sizes up to 150 µm was obtained by Huan Fushel Technology Limited (Hunan, China). **Table 1** lists the chemical composition of both powder materials measured by optical emission spectrometry (OES), carrier hot gas extraction (see Section 2.2.2), and the additivated powder as demonstrated in.[18,19] The additivation of Si_3N_4 powder to X2CrNi18-9 was adjusted as described in[18] to reach the maximum nitrogen content without forming nitrides or other brittle phases. A maximum theoretical nitrogen content of 0.45 wt% was targeted.

2.1.2. Reference Material

The reference material used in this study was a conventionally produced X2CrNiN18-9 alloy, supplied by Dongguan ZhaoFeng Metal Co., further named as 304LN. The chemical composition of the material was provided in Table 1. The material was solution annealed at 1160 °C for 20 min, followed by quenching in water.

2.2. Methods

2.2.1. Specimen Production

Specimen production was performed on a Realizer SLM 100 system (ReaLizer GmbH, Borchen, Germany) equipped with a pulsed Ytterbium fiber laser with a maximum laser power of 200 W at a wavelength of 1070 nm and a rotating powder spreading system. Constant process conditions were used containing a preheating temperature of 200 °C, an N_2 atmosphere, 50 µm layer thickness, and a shell-core scanning strategy. The details of the shell-core scanning strategy can be seen in **Figure 3**, for the example of a cuboid.

The scanning strategy comprises two distinct regions: the top/bottom area and the outline/core area. For the top and bottom regions, a stripe scanning strategy was implemented, utilizing a stripe length of 2.7 mm, a stripe width of 2.0 mm, a hatch distance of 0.1 mm, and a rotating hatch angle of 67°. Each region spans a height of 1 mm, achieved by printing 20 layers. The volume energy density (VED), can be adjusted by modifying the laser power and scanning speed. Between the top and bottom regions lies the outline/core area, which employs two laser

Table 1. Chemical composition of the used materials.

Material	Chemical composition [wt%]								
	C	Si	Mn	P + S	Cr	Ni	N	O	Fe
X2CrNi18-9[a)]	<0.03	0.85 ± 0.15	1.3 ± 0.16	<0.03	18.92 ± 0.27	9.11 ± 0.72	0.084 ± 0.01	0.03 ± 0.005	Bal.
Si_3N_4[a)]	–	Bal.	–	–	–	–	40.2 ± 0.36	0.7	–
X2CrNi18-9 + Si_3N_4[b)]	<0.03	1.39	1.29	<0.03	18.75	9.03	0.45	0.03	Bal.
X2CrNiN18-9[c)]	0.021	0.30	1.17	<0.03	18.25	8.03	0.12	–	Bal.

[a)]measured; [b)]calculated; [c)]given by data sheet.

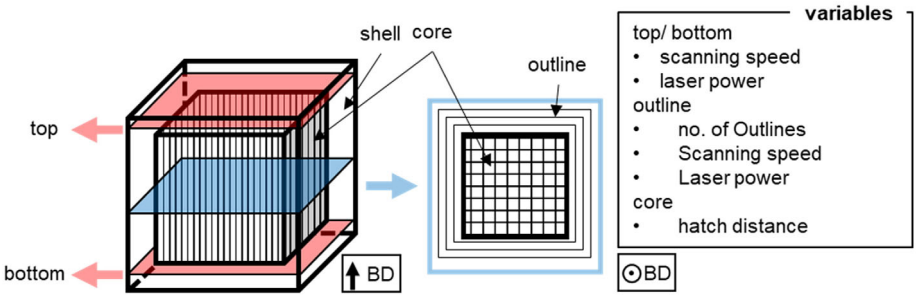

Figure 3. Visualization of the shell-core scanning strategy with an outline of the PBF-LB/M process variables on a cuboid sample.

scanning strategies. The first strategy, outline, defines the shell structure of the specimens, employing a fixed hatch distance of 0.1 mm. Both VED and the number of outlines can be adjusted in this strategy. Within the outline region lies the core structure, designed with a porous layout to maximize the retention of undissolved Si_3N_4 particles. For the core, the laser power and scanning speed were set at 180 W and 857 mm s^{-1}, respectively, while the hatch distance is adjustable and directly correlates with the porosity of the specimens.

HIP densification and integrated solution annealing were performed using a Quintus QIH9 HIP unit equipped with an integrated gas cooling function (URQ) achieving cooling rates up to 1000 K min^{-1}. The samples were consolidated at an argon pressure of 150 MPa and a temperature of 1200 °C for a total of 5 h and then quenched with an argon gas pressure of 100 MPa. The capsule, which was required for the PM + HIP sample production, was made of X2CrNi18-9 material. In addition, the cylindrical AM samples were also encapsulated to ensure the densification and alloy formation.

2.2.2. Chemical Composition

The chemical composition of the samples was measured by OES with a SPECTROMAXx LMX07 (SPECTRO Analytical Instruments GmbH, Germany). Additionally, C, O, and N contents were determined separately using a CS analyzer Leco CS300 (Leco Instrument GmbH, Germany) as well as an ONH analyzer Bruker GALILEO G8 (Bruker Corp., USA).

2.2.3. Mechanical Testing

Vickers hardness testing (HV10) was conducted on specimens in accordance with DIN EN ISO 6507-1:2018-07. For each condition, at least five indents were placed on cross-sections along the building direction. Quasi-static tensile tests were performed with a testing velocity of 0.06 mm s^{-1} according to DIN EN ISO 6892-1:2020-06 (Zmart Pro, Zwick Roell AG). The utilized specimen geometry was a type B 5 × 30 according to DIN 50 125: 2021-08 and was obtained by machining of as-built cylinders. Rotating bending fatigue tests ($R = -1$) were conducted at a frequency of 57.5 Hz. After printing, the specimens were machined, manually longitudinal polished, and tested in accordance with DIN 50 113:2018-12 as well as DIN 50 100:2016-12 using the staircase method and evaluation according to Hück.[21,22]

2.2.4. Microscopy

Light optical microscopy (LoM) examinations of the microstructure were performed on an Axio Imager M2m microscope from Carl Zeiss Microscopy. A scanning electron microscope (SEM) of type JSM-6400 (JEOL Ltd.) was used to analyze the powder particles and the resulting powder mixture homogeneity, as well as the fracture surfaces of mechanical testing samples, and characterization of fracture causing defects using energy dispersive spectroscopy (EDS) detector. Also, the EDS detector was used for mappings of Si to analyze the Si_3N_4 dissolution and Si homogeneity. Becker et al.[23] showed a nitrogen dispersion calculation based on quantitative EDS mappings (Fe, Cr, and Si) and a minimization function of the chemical potential. Inverse pole figure (IPF) mappings were taken to analyze the GS of the microstructure. Electron backscatter diffraction (EBSD) mappings were taken to analyze the resulting phases. A Bruker D8 Advanced system was used for X-ray diffraction (XRD) measurements for the calculation of microstrain within the powder particles.

3. Results & Discussion

3.1. Different Processing Strategies and their Influence on the Resulting Microstructure

Two different process routes are considered in this work. One is a powder metallurgical HIP route (PM-HIP), the other is a combination of laser-based additive manufacturing (PBF-LB/M) and hot isostatic pressing for post-compaction and alloy formation (AM-HIP). For both processes, two PSDs of the Si_3N_4 additive are added to the base material X2CrNi18-9, resulting in different powder properties (**Table 2**).

As expected, pure X2CrNi18-9 exhibits the best powder properties in terms of flowability (FR_H), Hausner ratio (HR), and packing density (PD). As already described and discussed in,[18] the addition of Si_3N_4 powder particles significantly deteriorates the powder properties and thus also the processing of the powders using PBF-LB/M. The highest influence was addressed to fine nonspherical Si_3N_4 particles, increasing the surface roughness, agglomeration, and interarticular forces. For this reason, the Si_3N_4 powder was fractionated before mixing with the base powder. For the Si_3N_4 powder with a particle size between 36–71 µm, hereinafter referred to as "coarse", slightly inferior

Table 2. Powder properties of pure X2CrNi18-9 and two powder mixtures of X2CrNi18-9 and Si_3N_4 using Si_3N_4 PSDs of 36–71 µm (coarse) and smaller than 36 µm (fine).

Material		PSD [µm]	FR_H [s 50 g^{-1}]	AD [g cm^{-3}]	TD [g cm^{-3}]	HR	PD [vol.-%]
X2CrNi18-9	–	20–50	17.7	4.25	4.88	1.15	54
X2CrNi18-9	**+Si_3N_4**	36–1	18.2 ± 1.1	3.91	4.85	1.24	49
		<36	17.5 ± 0.8	4.19	4.92	1.19	53

The bold material marks the material to which the PSD refers. In the first row towards the X2CrNi18-9 material and in the third and fourth row towards the Si_3N_4 material.

powder properties are observed; however, good processability of the powder is still anticipated. Reflection measurements at a wavelength of 1070 nm also demonstrated that the addition of Si_3N_4 has no direct impact on energy absorption via laser irradiation.[18] In contrast, strong demixing effects, caused by a radial spreading process, and the separation of Si_3N_4 powders were observed, which were also captured in a discrete element simulation.[17,24] For the Si_3N_4 fraction smaller than 36 µm, hereinafter referred to as "fine", a mechanical mixing methodology must be employed to ensure a homogeneous distribution of particles while simultaneously improving the powder properties.[17] For the PM-HIP route, tap density has the greatest influence on the processing. Both fractions of the manufactured powder mixtures exhibit very similar tap densities compared to pure X2CrNi18-9, suggesting favorable HIP results.

The mixing of fine Si_3N_4 particles with X2CrNi18-9 powder through mechanical alloying using WC milling balls leaves traces on the metal powder particles. Furthermore, it can be assumed that local dislocations have formed due to plastic deformation, thereby increasing the internal stress within the powders. Based on this assumption, XRD measurements to obtain the microstrain were conducted on fresh X2CrNi18-9 powder and ball milled (BM) X2CrNi18-9 powder, seen in **Figure 4**. Phase analysis reveals a predominantly austenitic microstructure for both powder samples. In the case of the BM powder, a minor peak corresponding to the δ-ferrite (110) reflection is detected, which is addressed to rapid cooling during atomizing of the powder material and neglected at this point.

Comparing the γ (111) reflex for both powders in Figure 4a difference in the peak width can be seen that indicates an increase in the microstrain value. Typically, the microstrain value is divided into positive and negative components. The median of both components for the two powders obtained from Rietveld analysis are as follows: 1) **fresh** X2CrNi18-9: 0.0017, 2) **BM** X2CrNi18-9: 0.0024.

It is evident that the microstrain increases by ≈40%. Literature provides several methodologies to correlate microstrain with dislocation density, including one proposed by Williamson and Smallman,[25] which has been previously applied to other austenitic stainless steels.[26] Calculating the dislocation density yields a value that is doubled for the mechanically alloyed powder mixture containing fine Si_3N_4.

3.1.1. PM-HIP Sample Production of X2CrNi18-9 + Si_3N_4 Powder Mixtures

In a first step, three HIP capsules were filled with different powders: X2CrNi18-9; X2CrNi18–9 + Si_3N_4 (coarse); X2CrNi18-9 + Si_3N_4 (fine). The following **Table 3** displays the resulting

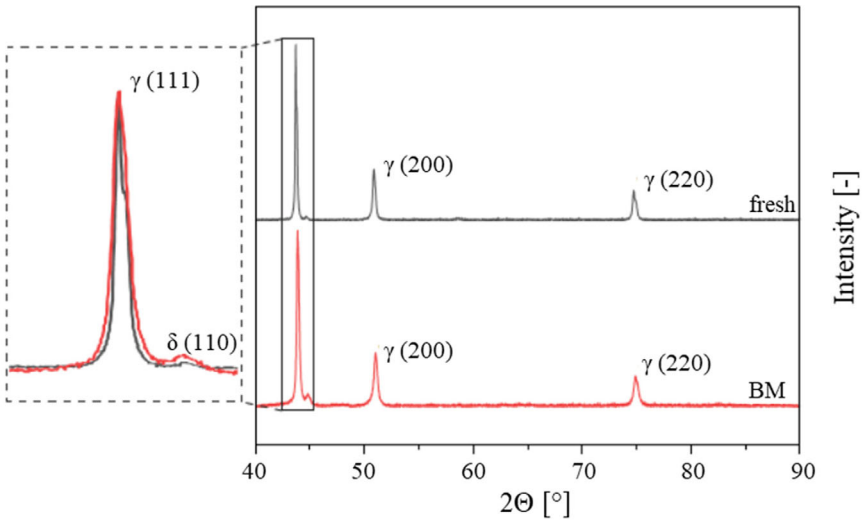

Figure 4. XRD spectrum of fresh X2CrNi18-9 powder and X2CrNi18-9 + Si_3N_4 (fine) powder mixture.

Table 3. N-contents measured by OES and GSs measured with EBSD of PM-HIP materials: X2CrNi18-9, X2CrNi18-9 + Si_3N_4 (fine), and X2CrNi18-9 + Si_3N_4 (coarse).

	X2CrNi18-9	+Si_3N_4 (coarse)	Si_3N_4 (fine)
N-content [wt.-%]	0.084	0.505	0.482
GS [μm^2]	78 ± 43	28 ± 16	44 ± 22

nitrogen contents of the consolidated material and the GS according to a median and a standard deviation.

The difference in nitrogen content between the two Si_3N_4 fractions appears negligibly small. The target amount was 0.5 wt.-%, with a minor nitrogen loss of 0.018 wt.-% observed when using the fine powder. A previous study,[16] which employed a Si_3N_4 fraction smaller than 150 µm (ultracoarse), showed a nitrogen loss of up to 0.38 wt.-% dissolved in the steel matrix. This loss is attributed to diffusion toward the gas atmosphere during the HIP processing.

The positive effect of twins on the Hall–Petch relationship in austenitic materials is well known.[27,28] This is why twin boundaries were also included as grain boundaries in the GS determination carried out here. The measured GS for the coarse additivated material is 28 ± 16 µm, indicating a significant refinement compared to the pure PM-HIP X2CrNi18-9 alloy (78 ± 43 µm). The GS of the microstructure obtained with fine Si_3N_4 particles exhibits an increased value of 44 ± 22 µm compared to that of the material with coarse Si_3N_4. This phenomenon can be attributed to two possible effects: 1) the introduction of dislocations through mechanical alloying; 2) the faster dissolution of small particles, reducing their impact on grain growth.[29] 1): As previously demonstrated, mechanical mixing enhances the microstrain within the powder, which correlates directly with dislocation density. It is already established that structural defects significantly influence sintering kinetics. In this context, the concept of structural activity of the material has been introduced, which accelerates the transport mechanisms relevant to sintering,[30] which can be transferred to the HIP process. Consequently, the energy stored within the material can be harnessed under specific temperature and time conditions to facilitate both sintering shrinkage and grain growth. 2): Ceramic Si_3N_4 particles act as grain growth inhibitors within the microstructure during HIP as long as they are partially undissolved. The larger the Si_3N_4 inclusions, the longer they persist undissolved in the microstructure, thereby effectively hindering grain growth. In contrast, finer particles dissolve faster during hot isostatic pressing, allowing for unimpeded grain growth and a faster homogenization of the microstructure. Currently, it remains unclear which mechanism ultimately contributes to such a pronounced difference in GS with respect to the varying sizes of Si_3N_4 particles. This presents potential for further investigation.

As reported in,[16] the Si distribution inside the steel matrix correlates directly to the interstitially dissolved N distribution. It is seen that complete silicon homogenization cannot be achieved via HIP using ultracoarse Si_3N_4 additives. Silicon diffuses too slowly, leaving Si-rich regions in the component. **Figure 5** shows qualitative Si-EDS mappings for three different PM-HIP materials: a) X2CrNI18-9, b) X2CrNi18-9 + Si_3N_4 (coarse), and c) X2CrNi18-9 + Si_3N_4 (fine) with the same result. In both Si_3N_4 particle size fractions in PM-HIP material, silicon-rich regions inside the steel matrix were detected, indicating insufficient diffusion time or temperature during the HIP process. However, the so-called diffusion zones appear significantly more homogeneous in samples with the finer PSD. which was also shown by Becker et al.[20] However, it does not ensure a fully uniform distribution of Si_3N_4 throughout the stainless steel matrix. The qualitative EDS mappings of silicon also reveal numerous bright spots corresponding to Si-rich oxides (SiO_2). These oxides, which persist after HIP processing, are also observed in the pure X2CrNi18-9 material. Due to the more uniform silicon distribution within the matrix, the Si-rich oxides exhibit a higher contrast. The finer Si_3N_4 PSD also promotes a more refined and widespread distribution of silicon-rich oxide inclusions, suggesting that particle size has a direct influence not only on diffusion behavior but also on the morphology and dispersion of oxide phases.

All presented materials confirm the formation of a fully austenitic microstructure (**Figure 6**), provided with numerous black points (unindexed regions). Due to the HIP densification process, a high level of porosity is unexpected. It is therefore assumed that these black points represent nonmetallic inclusions that either do not dissolve during HIP processing or are newly formed during the process. The literature reports that the HIP process not only facilitates the densification of samples but also promotes the formation of spherical oxides. So called prior particle boundaries form during HIP by breaking the thin oxide layers of the steel powder particles into fragments and forming spherical inclusions.[31–34] The use of fine Si_3N_4 particles may result in a similar effect. Due to their higher effective surface area, more oxygen is introduced into the system. During the HIP process, the thin oxide surface layers form numerous

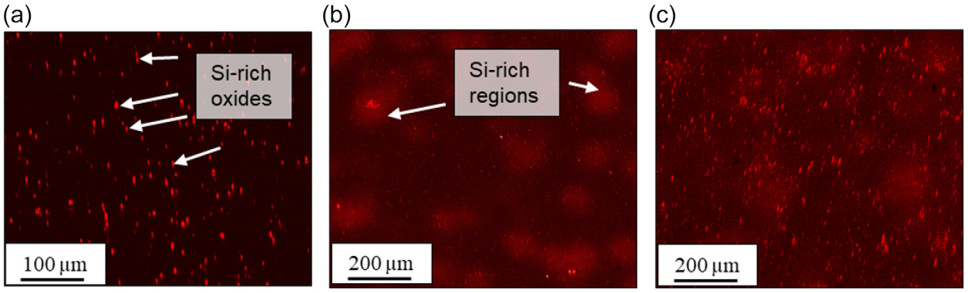

Figure 5. Qualitative Si-EDS mappings of PM-HIP materials: a) X2CrNi18-9, b) X2CrNi18-9 + Si_3N_4 (coarse), and c) X2CrNi18-9 + Si_3N_4 (fine).

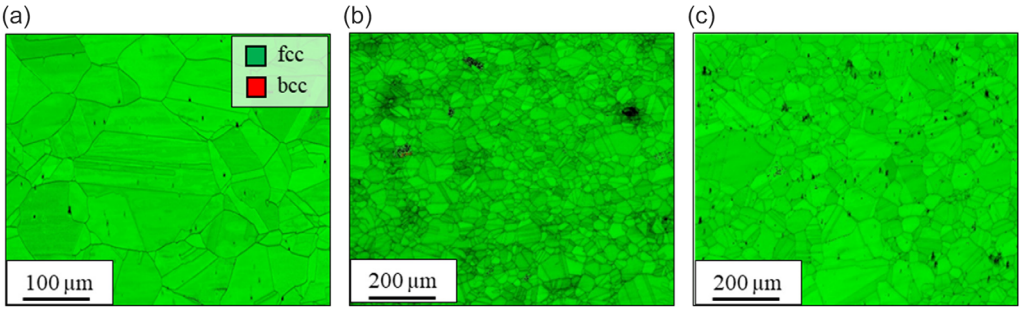

Figure 6. EBSD phase-mappings of PM-HIP materials: a) X2CrNi18-9, b) X2CrNi18-9 + Si_3N_4 (fine), and c) X2CrNi18-9 + Si_3N_4 (coarse).

small spherical oxides that cannot be dissolved. The impact of these oxide inclusions on the mechanical properties will be discussed later in the manuscript. Oxygen measurements of both particle fractions underline the high amount of integrated oxygen. The oxygen content listed in Table 1 represents the total amount of oxygen across the entire Si_3N_4 fraction. The fractionation of the powder suggests that finer distributions with an increased specific surface area may also carry a higher oxygen content. When considered individually, the fine Si_3N_4 powder contains less oxygen (7300 ppm) than coarse Si_3N_4 powder (8800 ppm), exactly the opposite of what was expected. This leads to the conclusion that the oxygen content can be introduced not only through oxygen-rich surfaces but also through individual oxide particles present in the powder. A fine Si_3N_4 fraction would thus also result in a finer oxide fraction, which decreases the overall amount of oxygen.

The GS, Si-rich regions, and oxide formation are considered potential influencing factors on the properties being evaluated. Consequently, in addition to the varying nitrogen content, the macroscopic observations will also need to be part of the discussion.

3.1.2. AM-HIP Sample Production of X2CrNi18-9 + Si_3N_4 Powder Mixtures Using the Shell-Core Scanning Strategy

For the upcoming investigations, two different sample geometries have been fabricated. On one hand, as shown in Figure 3, cube samples (cuboids) with dimensions of $10 \times 10 \times 10\,mm^3$ were produced. These samples are intended for a parameter study of a dense shell with the highest possible proportion of undissolved Si_3N_4 particles in the core. To achieve this, the number of outer layers and the VED of the shell, as well as the hatch distance in the core, were varied. All samples with a closed porosity are densified through HIP-URQ. Following this, microstructural investigations, nitrogen measurements, and hardness tests will be conducted on successfully densified samples and discussed together.

The second sample geometry consists of cylindrical samples with a radius of 10 mm and a height of 60 mm. The parameters for this sample geometry arise from the preceding parameter study. From the cylindrical samples, both tensile specimens and fatigue testing specimens will be manufactured and subsequently tested. In this case as well, a correlation between mechanical properties, microstructure, and nitrogen content will be established.

The following figure presents three cross-sections of shell-core samples manufactured using the PBF-LB/M process, where a dense shell structure could not be achieved. These cross-sections exemplify the changes in the process concerning the resulting defect structure.

Figure 7a shows the initial attempt of sample production using X2CrNi18-9 and coarse Si_3N_4 powder with a wall thickness of four outlines (≈0.4 mm). The marked areas indicate regions where defects break through the gas-tight shell, hindering HIP post-densification. It is evident that even small defects in the shell significantly affect the gas-tightness of the shell structure.

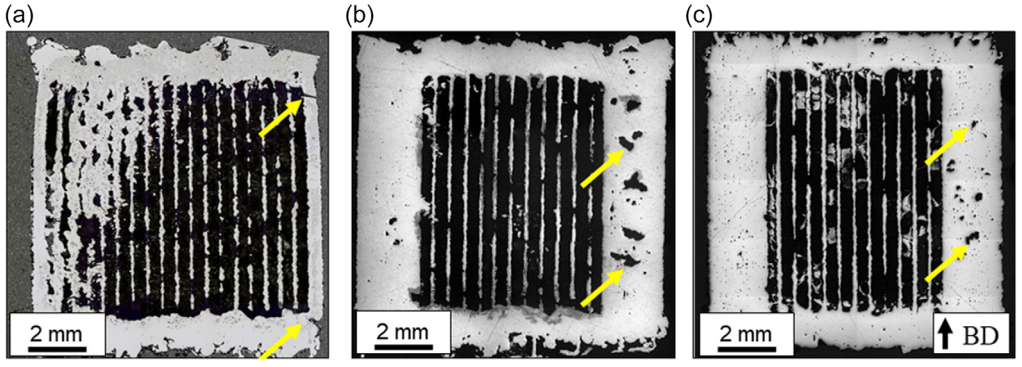

Figure 7. Cross-section images (LoM) of a) X2CrNi18-9 + Si_3N_4 (coarse) using 4 outlines, b) X2CrNi18-9 + Si_3N_4 (coarse) using 20 outlines, and c) X2CrNi18-9 + Si_3N_4 (fine) using 20 outlines.

No problematic defects were ever detected in the bottom or top structure. Consequently, samples with an increased outline quantity were produced. Figure 7b displays a sample made from identical powder and process parameters but with a shell five times thicker (≈2.0 mm). When examining the cross-section, it becomes clear that as wall thickness increases, so does defect size. A comparison between the right and left sides also clearly shows that defect formation has a certain degree of statistical variability. As previously investigated in,[18] Si_3N_4 particles negatively affect both flow properties and melting behavior, which promotes defect formation in the component. For this reason, finer Si_3N_4 particles have been considered in the present work. Previous results have already shown that using fine Si_3N_4 as an additive improves powder properties as well as positively influences microstructure and diffusion behavior. In the third cross-section image presented, it is clearly visible that while the number of defects cannot be reduced, their size can be significantly minimized. These defects continue to suggest that fine Si_3N_4 particles decompose during processing and promote the formation of bonding defects, lack of fusion defects, and gas pores,[18] although these defects are formed much finer. By reducing defect size, the statistical reliability of a gas-tight shell is greatly enhanced. All of the gas-tight samples were HIP post-densified to a density of ≈99.99 vol.-% and the nitrogen content was measured. Besides the shell scanning parameters, also the hatch distance and scanning strategy of the core samples were varied. In addition to the number of outlines, a different amount of Si_3N_4 particles should retain in the core resulting in different nitrogen contents between 0.193 wt.-% and 0.287 wt.-%. In general, it can be assumed that only the powder areas not in contact with the laser consist of nitrogen-rich Si_3N_4 particles, which can lead to solid solution strengthening. For the laser-exposed areas, nitrogen outgassing and pore formation will occur, which must be reduced to a pore amount that is not critical for HIP.

Next to the nitrogen content, there is also a strong impact on the microstructure due to the scanning strategy. The following **Figure 8** shows a successfully compacted sample (a), a scanning electron microscopy image (b), and an IPF map (c) of a PM-HIP-processed coarse Si_3N_4 powder mixture.

The densification is clearly evident by the shrinkage of the sample. Due to the internal porosity, the walls collapse, resulting in the shrinkage of the sample. In the SEM image, a distinction can be made between the shell-area and the core-area based on their positioning. As already noted in,[19,29] the core-area further varies into an AM-compacted region (struts) and a HIP-compacted region (powder). The HIP-compacted region can be distinctly identified by inclusions that form as a result of the HIP process from the oxide skins of the powder particles (PPB), leaving spherical oxide inclusions. In contrast, these inclusions are not visible in the AM-compacted region.

Although a fine microstructure is typically expected after the AM process,[7] the subsequent HIP treatment leads to significant grain coarsening. As a result, GSs in the AM-compacted regions are larger than those in conventionally HIP-compacted areas. Another key difference is the presence of undissolved Si_3N_4 particles, which are observed exclusively in the powder-based regions. From these regions, the particles gradually diffuse into the surrounding matrix during HIP consolidation. Due to the narrower geometry of the "struts" compared to the "shell", and the associated nitrogen loss at the component edges, a subtle nitrogen gradient is observed toward the outer regions.[19] Since nitrogen has a grain-refining effect,[4] this gradient explains the finer grain structure observed in the core relative to the shell. Through targeted adjustment of the scanning strategy and the arrangement of the struts, it is possible to directly influence the quantity of undissolved Si_3N_4 particles retained after AM processing, and thereby indirectly control the resulting GS after the HIP consolidation.

For the coarse Si_3N_4 powder, an average GS of 17+/−14 µm[19] µm has been determined, while for the fine powder, an average GS of 20+/−15µm[29] was measured in the core area. The trend toward a finer grain structure with coarse Si_3N_4 powder is also recognized, as already shown in Table 3 for the PM-HIP material.

3.2. Investigation of the Mechanical Properties

Due to many different combinations for sample production and testing, the following **Table 4** summarizes all characterizations made for this section. The colors represent the PSD of Si_3N_4 additive, and the symbols represent the different types of fabrication.

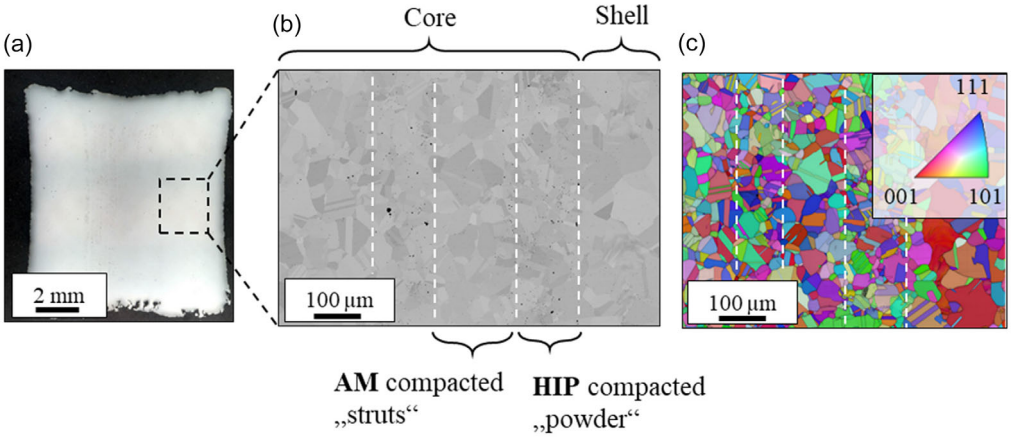

Figure 8. AM- and HIP-compacted X2CrNi18-9 + Si_3N_4 (coarse) shell-core sample: a) LoM cross-section. b) SEM close-up. and c) IPF-map.

Table 4. Summary of all mechanical tests in relation to their process route and Si_3N_4 PSD.

Process	Si_3N_4 PSD	Symbol	Naming	Hardness	Tensile	Fatigue
Metallurgy	–	▲	Ref.	+	+	+
PM-HIP	–	●	PM	+	+	+
PM-HIP	Coarse	●	PM_Coarse	+	+	+
PM-HIP	Fine	●	PM_Fine	+	+	+
AM-HIP	Coarse	■	AM_Coarse	+	–	–
AM-HIP	Fine	■	AM_Fine	+	+	+

3.2.1. Hardness Test Results

The following diagram in **Figure 9** presents the measured hardness values of all samples as a function of the measured nitrogen content.

The lowest hardness value of 157 ± 6 HV10 was measured for the X2CrNi18-9 PM-HIP material with the lowest nitrogen content of 0.084 wt%. An increase in nitrogen content by ≈0.04 wt% leads to an increase in hardness to 162 ± 3 HV10. Notably, the values for the metallurgically produced X2CrNiN18-9 material exhibit lower scatter. The addition of Si_3N_4 enables exceeding the solubility limit (N: ≈0.12 wt%) for nitrogen in the liquid phase, which, as shown in the diagram, is clearly associated with a nearly linear increase in hardness.

The lowest nitrogen uptake was observed when using coarse Si_3N_4 additive in the AM-HIP process, where nitrogen levels between 0.193 and 0.287 wt% were achieved, leading to hardness values of 170 HV10 to 190 HV10. The use of fine Si_3N_4 as an additive resulted in a significantly higher-nitrogen content, with values between 0.277 and 0.460 wt% being realized. This result clearly indicates that segregation effects play a crucial role in the processing of powder mixtures especially with different particle sizes.[17,35,36] Köhler et al.[37] demonstrated that coarse additives settle at the bottom of the build plate or get pushed over the building platform, and fine particles fall into the powder bed at the beginning of the recoating. The same phenomena were observed with the addition of coarse Si_3N_4,[18] so mechanical alloying of fine Si_3N_4 was used to mechanically bond the two types of powder. The rotating powder spreading process plays a critical role in segregation phenomena and should be considered a key factor in material inhomogeneity. In addition to variations in the chemical composition during the process, this naturally leads to fluctuating mechanical properties. The measured hardness values range from 185 HV10 to 230 HV10. Around a nitrogen content of 0.3 wt%, the hardness values of both additives overlap for AM-HIP-processed samples.

This influence becomes more apparent when examining PM-HIP samples. For both PSDs, samples with an increased nitrogen content of around 0.5 wt.-% were tested. The use of fine Si_3N_4 resulted in lower hardness values with a higher standard deviation of 213 ± 9 HV10, whereas coarse Si_3N_4 led to a hardness of 229 ± 4 HV10. This increase can be explained by variations in nitrogen content of 0.023 wt.-%. As previously shown and discussed in Figure 5, the GS in the microstructure differs significantly depending on the Si_3N_4 PSD, which will be discussed later.

This result clearly demonstrates that, in addition to the introduced nitrogen content, the resulting microstructure has a significant impact on the mechanical properties. Future research must focus on understanding how the selected additives influence microstructural evolution.

3.2.2. Tensile Test Results

Tensile tests were conducted on five different sample conditions. **Figure 10** shows the resulting stress–strain curves for one example of each condition.

The stress–strain curves each condition show minimal differences, making the consideration of a single specimen per condition sufficient for a qualitative comparison. As described by Gavriljuk and Berns,[4] nitrogen atoms complicate the dislocation movement, thereby enhancing the strength of the Fe-based material.

Reference Material: The PM-HIP reference condition of the X2CrNi18-9 material exhibits the lowest tensile strength at 626.16 ± 0.33 MPa while achieving the highest elongation at break with 75.74 ± 0.74%. The relatively low nitrogen content

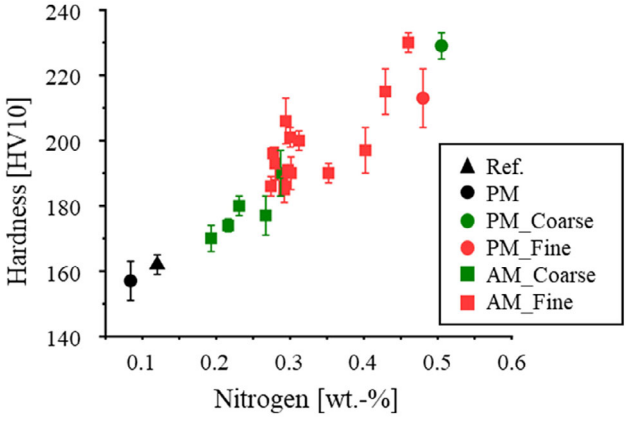

Figure 9. Hardness values in dependence on the nitrogen content due to different processing routes.

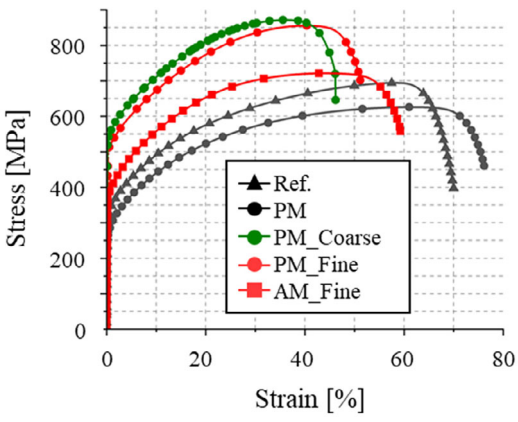

Figure 10. Stress–Strain curves for five exemplary samples in different process routes.

explains the comparatively low strength, while the homogeneous HIP microstructure of the austenitic material contributes to the highest elongation at break. The material data sheet for conventionally manufactured X2CrNi18-9 specifies a minimum elongation at break of 45% in the longitudinal direction and 35% in the transverse direction. The comparison with the HIP-processed material clearly highlights the influence of the high-purity HIP microstructure and demonstrates the advantages of the HIP route. According to the data sheet, the tensile strength is limited to a maximum of 700 MPa, which closely matches the value of the metallurgically produced X2CrNiN18–9 (692 ± 6 MPa).

AM-HIP: The AM-HIP materials exceed the maximum solubility limit of nitrogen in the liquid phase of X2CrNi18-9 ($N = 0.277$–0.312 wt.-%), leading to an ultimate tensile strength (UTS) of 723 ± 2 MPa. Despite the inherent variability of the AM and hot isostatic pressing (AM-HIP) process, the mechanical properties of the samples are highly consistent, suggesting a certain degree of process stability. The influence of nitrogen on the mechanical properties is discussed in greater detail in the following sections. With increasing strength, elongation at break decreases but never falls below the required 45% specified value in the material data sheet for conventional X2CrNi18-9.

PM-HIP: The powder metallurgical HIP route for X2CrNi18-9 + Si_3N_4 leads to a significant increase in strength. The material with coarse Si_3N_4 additive reaches a maximum tensile strength of 868 ± 2 MPa. As already observed in the previous Figure 10, a small variation in strength and elongation of the PM-HIP material depending on the Si_3N_4 particle size can be identified. This effect can again be attributed to the formation of a finer grain structure when using coarse Si_3N_4, with grain refinement mechanisms contributing to increased material strength. Notably, this effect results in only a minor increase in tensile strength of +13 MPa (+1.5%) but has a more pronounced effect on the reduction of elongation at break by −5% (−9%). The negative effect of nitrogen on the ductility was also seen by Boes et al.[14] addressed to the high microstructural defect density.

For a more detailed analysis, the three characteristic material properties yield strength (YS), UTS, and elongation at break (At_5) are plotted against the respective nitrogen content for all tested samples in the following section.

To gain a deeper understanding of the influence of nitrogen on the characteristic values of the tensile test, three diagrams are plotted in **Figure 11**. The diagrams show the YS Figure 11a**)**, UTS Figure 11b), and elongation at break (At_5) Figure 11c) for each tested sample along with the corresponding nitrogen

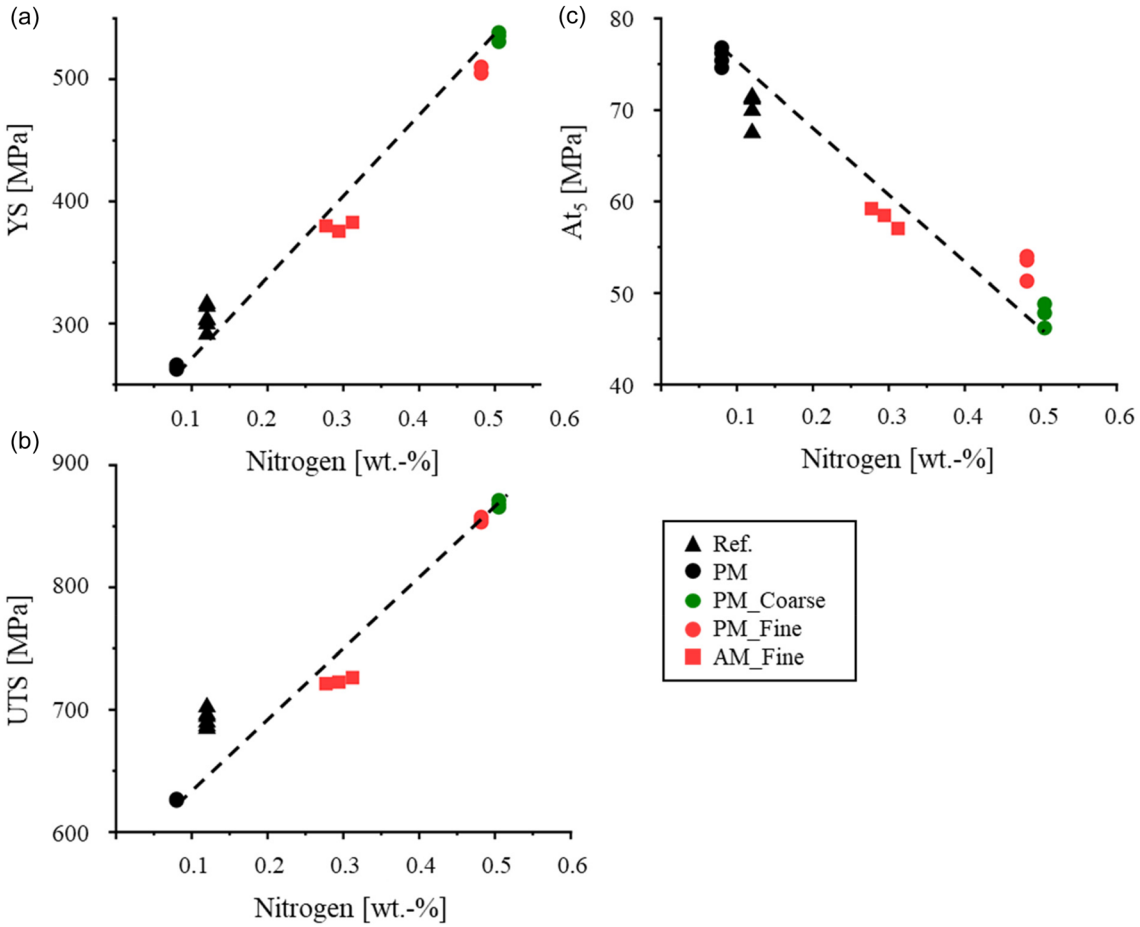

Figure 11. Characteristic properties a) YS. b) UTS (b). and c) elongation at break (At_5) plotted over the nitrogen content due to different processing routes.

measurement values. For all data, a fit between minimum and maximum nitrogen content has been drawn, as a linear increase with rising nitrogen content was expected, similar to hardness values as seen in Figure 9. Wang et al.[38] also observed an increase in strength values with rising nitrogen content. By maintaining a constant GS, they were able to isolate the nitrogen-induced strengthening effects, which were attributed to planar slip, stacking fault formation, and solid solution strengthening.

YS: It is evident for YS that the addition of fine Si_3N_4 for both AM-HIP and PM-HIP variants lies below the linear trend. The best results are thus obtained from using coarse Si_3N_4 particles. Comparing the three red squares makes it clear that no distinct trend is recognizable within a manufacturing route for different nitrogen contents. The significant differences in PSD used in the PM-HIP process have already been recognized. Wang et al.[38] published a relationship between the nitrogen content and the Hall-Petch[39] factors K (strengthening coefficient) and σ_0 (material constant), to directly connect all material characteristics in one formula for a PESR 316L material. GS was found to be a relevant factor up to ≈100 µm, beyond which only the nitrogen content contributes significantly to the Hall–Petch relationship. The strengthening effect of nitrogen becomes increasingly dominant at higher concentrations, with the maximum reported content of 0.34 mass-%. This is further reflected in enhanced twin formation, planar slip behavior, stacking fault generation, and solid solution strengthening mechanisms. In the samples analyzed within this study, GSs were consistently below 100 µm, indicating that GS effects on YS must be accounted for. Since the nitrogen content exceeds 0.34 mass-%, an even stronger influence of nitrogen is assumed. Based on the modified Hall–Petch relationship proposed by Wang et al., and using the experimentally determined GSs, the following YS values were calculated for the two PM-HIP Materials: 1) YS (PM-HIP_Coarse) = 587 MPa, 2) YS (PM-HIP_Fine) = 515 MPa.

For the PM-HIP_Fine material, the calculated hardness values showed good agreement with the experimental results, with a deviation of 7 MPa. In contrast, the YS of the PM-HIP_Coarse material was slightly overestimated, suggesting a potential underperformance of the actual material. This discrepancy may be attributed to the broader PSD (as shown in Table 3) or slight inhomogeneities in nitrogen distribution.

UTS: A strong influence of the manufacturing route can be observed for UTS. Here, samples in Table 4 produced via melting metallurgy lie significantly above what would be expected from a linear trend. Again, AM-HIP samples lie distinctly below; although they show a considerable increase in nitrogen content, they do not massively affect UTS. However, within the three samples with increasing nitrogen content, a consistent rise in UTS can be observed. The increased UTS with higher-nitrogen uptake in AM samples has been observed in several publications,[2,14,40,41] and is attributed to solid solution strengthening. This effect operates independently of the production route and Si_3N_4 PSD, although small differences are still evident. The difference regarding particle sizes used in the PM-HIP process is much smaller; here, the influence of nitrogen is much clearer as a perfect linear assumption. The change in GS does not seem to affect the UTS as strongly, as there are no outliers. This indicates that nitrogen as an alloying element has a significant impact on tensile strength, which can be attributed to an increased dislocation density caused by the nitrogen uptake.[41,42]

Elongation at Break: For elongation at break, an almost linear trend can be seen across all samples; the influence of the manufacturing process is minimal, while AM-HIP samples slightly overperform. This can be attributed to lower strength since ductility prevails in these samples accordingly. Also, for these parameters, there is a consistent decrease in elongation at break with increasing nitrogen content within AM-HIP samples. The influence of GS for different Si_3N_4 particle sizes also becomes evident: fine Si_3N_4 leads to coarse microstructures, which enhance elongation at break. Accordingly, an almost linear relationship between elongation at break and nitrogen dependency can be assumed when identical GSs are considered. In contrast to the findings of Wang et al.[38] no plateau was observed for a specific nitrogen content. This discrepancy can be attributed to the use of different processing routes in the present study.

The results of the tensile tests clearly demonstrate a linear influence of nitrogen content on the characteristic values. However, it is essential to also consider the production route and the corresponding microstructure when discussing these results. Nevertheless, all additivated powder samples surpass the UTS and elongation at break of standard X2CrNi18-9 values. With an increase in nitrogen content, both the YS and UTS exhibit a nearly linear increase, while the elongation at break decreases linearly.

3.2.3. Fatigue Test Results and Fracture Surface Analysis

Fatigue tests were conducted to identify the characteristic fracture inducing defects. To identify the failure mechanisms and material properties, S/N curves for high-cycle fatigue were generated, without a specific focus on long-life fatigue behavior. The first diagram (a) presents the test results for the three different PM-HIP materials. For clarity, a second diagram has been created that illustrates the high-cycle fatigue behavior limit and summarizes the measurement points of the melt-metallurgical reference material along with those of the additively manufactured samples (b).

A comparison of the PM-HIP materials (a) clearly shows the significant influence of nitrogen on the high-cycle fatigue strength of the samples. In the reference condition no number of cycles higher than 10 000 (reliable number of cycles) could be obtained for a stress amplitude of 350 MPa. For 250 MPa, one sample was tested without rupture, which means that the specimen reached more than the specified ultimate number of cycles of 10^7. The HNS materials exhibit reliable cycle counts ($N > 10\,000$) up to stress amplitudes of 500 MPa. A comparison of the two Si_3N_4 particle sizes again demonstrates an influence on mechanical durability. Unlike what was observed for hardness and tensile strength values, the fine PSD of Si_3N_4 shows higher long-life fatigue performances.

For nearly all samples, multiple fatigue crack initiation sites were observed at the specimen surface. This phenomenon is also well known from literature,[43,44] which often describes the absence of a singular, dominant crack origin in austenitic steels. Due to the relatively soft and ductile nature of the material, high testing frequencies can lead to rapid temperature increases as a

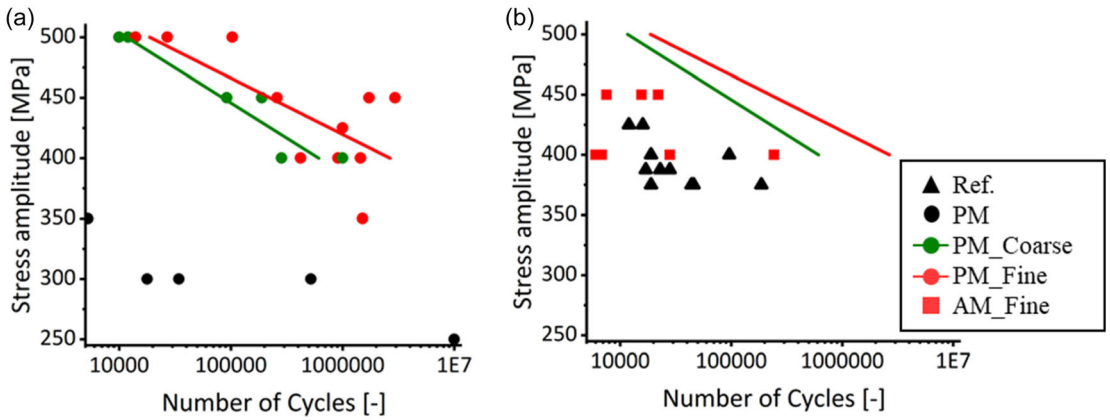

Figure 12. S–N curves of the rotating bending test for a) PM-HIP X2CrNi18-9, X2CrNi18-$+Si_3N_4$ (coarse), and X2CrNi18-$+Si_3N_4$ (fine) and b) X2CrNiN18-9 and AM-HIP X2CrNi18-$+Si_3N_4$ (fine).

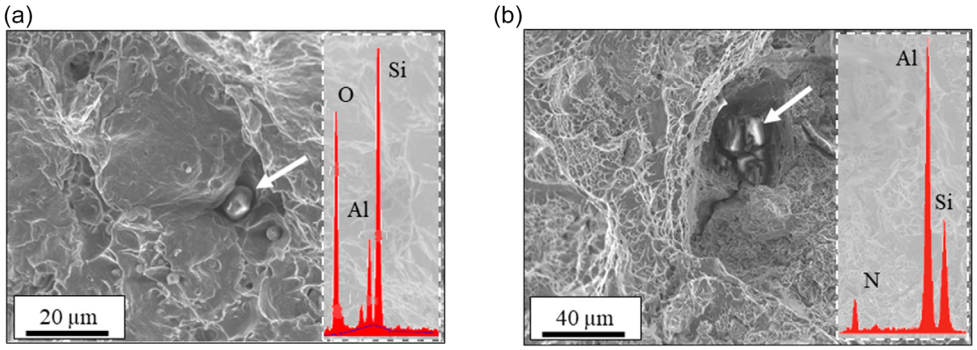

Figure 13. SEM images of fracture surface and EDS scan of inclusions for PM-HIP-processed samples with a) the mixture of fine Si_3N_4. and b) the mixture of coarse Si_3N_4.

result of internal friction and plastic deformation. To mitigate this effect, all fatigue tests were conducted at a moderate frequency of 57.5 Hz. The presence of multiple surface-initiated cracks results in fracture surfaces that exhibit characteristic fatigue progression zones near the specimen edge, distributed circumferentially. Toward the center of the fracture surface, a typically round region of final overload failure can be identified. A detailed fractographic analysis of these final fracture regions is presented in **Figure 12**, comparing two Si_3N_4 PSDs after PM-HIP processing. The specimen shown in Figure 12a failed at an applied stress of 500 MPa after 27 000 cycles, whereas the specimen in Figure 12b failed under the same stress level after only 12 000 cycles. In both cases, significant amounts of nonmetallic inclusions were identified within the overload fracture zone, suggesting a critical role in the premature failure mechanism **Figure 13**.

The measured nonmetallic inclusions are mostly Si-Al-*O*-N compounds. As noted in the microstructural investigation, the Si_3N_4 powder introduces a certain level of contamination into the system. The high-melting Si-Al compounds cannot dissolve during the HIP process and remain as inclusions in the component. Fractionation of the powder before processing also fractionates these introduced oxidic particles. Consequently, samples containing fine Si_3N_4 particles also show finer inclusions. Furthermore, when comparing the two types of inclusions presented, it is evident that fine inclusions have a higher circularity and consequently a smaller notch radius. In contrast, large inclusions are often characterized by already fractured particles, which promotes crack formation. Thus, the fractionation of Si3N4 particles has two positive effects on long-life fatigue strength: 1) Reduction in the size of oxidic inclusions; 2) Reduced notch effect due to a higher sphericity of the small inclusions.

4. Conclusion and Outlook

4.1. Conclusion

A nearly linear correlation was observed between nitrogen content and mechanical properties such as hardness, UTS, YS, and elongation at break. Minor deviations in the results can be attributed to microstructural factors like GS, which are influenced by the specific production route. Nevertheless, nitrogen content was shown to have a largely independent and dominant effect on these properties. Using the individual calculation of Hall–Petch law by Wang et al.[38] the YS could be accurately predicted based on nitrogen content and GS. This is addressed to the

effects of nitrogen toward planar slip, stacking fault formation, and solution strengthening.[4,45–47]

The fabrication of specimens using different powder metallurgy (PM) routes, aimed at achieving varying nitrogen contents and GSs, has yielded numerous practical insights. In the context of PBF-LB/M processing, the following observations were made: 1) The use of fine Si_3N_4 in the PBF-LB/M process also leads to a high number of statistically distributed defects, as has been documented for larger particle sizes. 2) It was possible to reduce the defect size, which increased the probability of producing a gas-tight shell. 3) Depending on the scanning strategy, it is possible to vary nitrogen content within the samples.

The shell-core scanning strategy yielded only moderate results in the present study. Currently, the introduction of nitrogen via powder mixtures with Si_3N_4 in the PBF-LB/M process does not yet offer sufficient process stability and a too high defect density, which has not yet made reproducible manufacturing of gas-tight samples possible.

The PM-HIP route successfully demonstrated the upper limit of this approach. Furthermore, initial findings regarding the influence of Si_3N_4 particle size on dissolution behavior and final microstructure have been obtained: 1) Fine Si_3N_4 results in increased GS compared to coarse Si_3N_4. 2) Fine Si_3N_4 reduces the size of nonmetallic inclusions and the amount of oxygen within the component and therefore also the long-life fatigue behavior.

4.2. Outlook

Within the PM-HIP material group, a clear influence of Si_3N_4 particle size and the applied mixing method on the resulting GS was observed. The next logical step involves a systematic investigation of this relationship through extended experimental studies, incorporating a broader range of PSDs. Additionally, detailed microstructural analysis should be conducted to assess the impact of ball milling on dislocation density, which may further influence grain growth or diffusion behavior. Complementary diffusion simulations could provide valuable insight by estimating the time required to achieve a homogeneous silicon distribution as a function of Si_3N_4 PSD. Further reduction of the PSD and an increase in purity through the use of Si_3N_4 nanoparticles (NP) could also have positive effects on the process chain. Currently, Si_3N_4 NP's are used merely as additives to improve powder properties[48,49] without considering their influence on the final chemistry of the component.

For the AM-HIP materials, the most significant challenge in the current process chain is the reproducible AM of gas-tight shells. Addressing this issue, further investigations regarding varying parameter studies need to be conducted. The current state of research is focused on reducing energy peaks through so-called beam shaping[50,51] or the use of ultrashort pulsed laser systems.[52] The use of such systems could also have a positive effect on the utilization of powder mixtures, as the main problem lies in Si_3N_4 dissolution. Furthermore, a comprehensive study is required to evaluate the effect of varying scan strategies in shell-core architectures. This should focus on the local distribution of nitrogen and its impact on GS. Such an approach could enable the intentional design of highly anisotropic microstructures. Ultimately, the goal is to establish a direct and quantitative link between process parameters and resulting material properties.

Acknowledgements

The authors kindly acknowledge the financial support of the German Research Foundation (DFG) within the project 493947509 "Influence of an Si_3N_4 PBF-LB processability of stainless steels and the microstructure development during PBF-LB and subsequent HIP-URQ", which is part of the priority program SPP2122 "Materials for AM (MATframe)".

Open Access funding enabled and organized by Projekt DEAL.

Conflict of Interest

The authors declare no conflict of interest.

Author Contributions

Felix Radtke: conceptualization (lead); data curation (lead); formal analysis (lead); investigation (lead); methodology (lead); validation (lead); visualization (lead); writing—original draft (lead). **Louis Becker**: conceptualization (supporting); data curation (equal); formal analysis (supporting); investigation (supporting); validation (supporting); visualization (supporting); writing—review and editing (supporting). **Lars Schultze-Schlutius**: data curation (supporting); formal analysis (supporting); writing—original draft (supporting); writing—review & editing (supporting). **Anke Kaletsch**: conceptualization (equal); methodology (equal); project administration (equal); supervision (equal); writing—review and editing (supporting). **Jonathan Lentz**: conceptualization (supporting); methodology (supporting); project administration (equal); supervision (equal); writing—review and editing (supporting). **Sebastian Weber**: conceptualization (equal); funding acquisition (lead); resources (lead); supervision (lead). **Christoph Broeckmann**: conceptualization (equal); funding acquisition (lead); resources (lead); supervision (lead); writing—review and editing (supporting).

Data Availability Statement

The data that support the findings of this study are available from the corresponding author upon reasonable request.

Keywords

additive manufacturing, high-nitrogen austenitic stainless steels, hot isostatic pressing, powder mixtures, silicon nitrides

Received: March 31, 2025
Revised: May 13, 2025
Published online:

[1] B. D. Shanina, V. G. Gavriljuk, H. Berns, *Steel Res. Int.* **2007**, *78*, 724.
[2] T. V. Rashev, A. V. Eliseev, L. T. Zhekova, P. V. Bogev, *Steel Transl.* **2019**, *49*, 433.
[3] J. W. Simmons, *Mater. Sci. Eng.: A* **1996**, *207*, 159.
[4] V. G. Gavriljuk, H. Berns, *High Nitrogen Steels* **1999**, 5.
[5] R. Hasenhündl, S. Eglsäer, H. Orthaber, R. Tanzer, W. Schützenhöfer, R. Schneider, *Berg- Huettenmaenn. Monatsh.* **2009**, *154*, 194.
[6] V. I. Dimitrov, K. Jekov, A. Avinç, *Comput. Mater. Sci.* **1999**, *15*, 400.
[7] S. R. Narasimharaju, W. Zeng, T. L. See, Z. Zhu, P. Scott, X. Jiang, S. Lou, *J. Manuf. Process.* **2022**, *75*, 375.

[8] X. Li, H. J. Willy, S. Chang, W. Lu, T. S. Herng, J. Ding, *Mater. Des.* **2018**, *145*, 1.
[9] W. Zhai, W. Zhou, Z. Zhu, S. M. L. Nai, *Steel Res. Int.* **2022**, *93*, 2100664.
[10] *Additive Manufacturing in Multidisciplinary Cooperation and Production*, (Eds: I. Drstvensek, S. Pal, N. Ihan Hren), Springer International Publishing, Cham **2024**.
[11] S. Qin, Y. Bo, S. Herzog, B. Hallstedt, A. Kaletsch, C. Broeckmann, *Powders* **2022**, *1*, 184.
[12] S. Malgave, P. Shanthappa, C. Polidas, A. Nagaraja, *J. Jpn. Soc. Powder Powder Metall.* **2025**, *72*, S395.
[13] *A PBF-LB/M Process for an Austenitic High Nitrogen Steel* (Eds: F. Radtke, M. Mirz, S. Herzog, K. Dollmeier, C. Broeckmann), EPMA, Brussels, Belgium **2024**.
[14] J. Boes, A. Röttger, L. Becker, W. Theisen, *Addit. Manuf.* **2019**, *30*, 100836.
[15] E. H. Valente, V. K. Nadimpalli, T. L. Christiansen, D. B. Pedersen, M. A. Somers, *Manuf. Lett.* **2021**, *1*, 100006.
[16] L. Becker, F. Radtke, J. Lentz, S. Herzog, C. Broeckmann, S. Weber, *Mater. Lett.* **2023**, *352*, 135119.
[17] F. Radtke, L. Becker, S. Herzog, J. Lentz, S. Weber, C. Broeckmann, *Lasers in Manufacturing Conference*, WLT, Suttgart, Germany **2023**.
[18] F. Radtke, L. Becker, N. Hantke, S. Herzog, J. Lentz, J. T. Sehrt, S. Weber, C. Broeckmann, *Powder Technol.* **2024**, *448*, 120289.
[19] L. Becker, F. Radtke, J. Lentz, S. Herzog, C. Broeckmann, S. Weber, *Manuf. Lett.* **2024**, *9*, 100205.
[20] L. Becker, F. Radtke, J. Lentz, S. Herzog, C. Broeckmann, S. Weber, *Proceedings*, EPMA, Euro **2024**, p. PM2024.
[21] DIN 50113:2018-12, Prüfung metallischer Werkstoffe_- Umlaufbiegeversuch, DIN Media GmbH, Berlin.
[22] DIN 50100:2022-12, Schwingfestigkeitsversuch_- Durchführung und Auswertung von zyklischen Versuchen mit konstanter Lastamplitude für metallische Werkstoffproben und Bauteile, DIN Media GmbH, Berlin.
[23] L. Becker, F. Radtke, J. Lentz, S. Benito, C. Broeckmann, S. Weber, *Adv. Eng. Mater.* **2024**.
[24] Y. Deng, Z. Sang, J. Zhang, F. Radtke, L. Becker, S. Herzog, S. Weber, C. Broeckmann, *Adv. Eng. Mater.* **2024**.
[25] G. K. Williamson, R. E. Smallman, *Philos. Mag.* **1956**, *1*, 34.
[26] S. Murugesan, P. Kuppusami, E. Mohandas, M. Vijayalakshmi, *Mater. Lett.* **2012**, *67*, 173.
[27] C. S. Pande, B. B. Rath, M. A. Imam, *Mater. Sci. Eng.: A* **2004**, *367*, 171.
[28] B. Q. Shi, Y. Q. Cheng, X. L. Shang, H. Yan, R. S. Chen, W. Ke, *Mater. Sci. Eng.: A* **2019**, *743*, 558.
[29] L. Becker, F. Radtke, J. Lentz, S. Herzog, C. Broeckmann, S. Weber, *Adv. Eng. Mater.* **2024**.
[30] P. Lányi, W. Hermel, *Powder Metall.* **1981**, *24*, 93.
[31] F. Javadzadeh Kalahroudi, F. Lin, P. Krakhmalev, M. Grehk, *Metals* **2024**, *14*, 1159.
[32] J. Li, Y. Ma, Q. Cai, W. Liu, Y. Duan, C. Liang, *JOM* **2022**, *74*, 3595.
[33] A. Kaletsch, F. Radtke, S. Herzog, P. Köhnen, S. Höges, C. Broeckmann, *Appl. Sci.* **2023**, *13*, 12676.
[34] F. Radtke, L. Becker, S. Herzog, J. Lentz, S. Weber, C. Broeckmann, *Euro PM2023 Proceedings*, EPMA, Brussles Belgium **2023**.
[35] M. H. Mosallanejad, B. Niroumand, A. Aversa, A. Saboori, *J. Alloys Compd.* **2021**, *872*, 159567.
[36] L. Shoji Aota, P. Bajaj, H. R. Zschommler Sandim, E. Aimé Jägle, *Materials* **2020**, *13*.
[37] M. L. Köhler, F. Ali, S. Herzog, P. Suwanpinij, A. Kaletsch, C. Broeckmann, *Steel Res. Int.* **2022**, *93*.
[38] Y. Wang, Z. Wang, W. Wang, B. Ma, *Mater. Sci. Eng.: A* **2023**, *884*, 145549.
[39] G. Gottstein, *Materialwissenschaft Und Werkstofftechnik*, Springer Berlin Heidelberg, Berlin, Heidelberg **2014**.
[40] F. Stern, L. Becker, C. Cui, J. Tenkamp, V. Uhlenwinkel, M. Steinbacher, J. Boes, J. Lentz, R. Fechte-Heinen, S. Weber, F. Walther, *Adv. Eng. Mater.* **2022**, *25*.
[41] N. Hansen, *Scr. Mater.* **2004**, *51*, 801.
[42] O. O. Salman, C. Gammer, A. K. Chaubey, J. Eckert, S. Scudino, *Mater. Sci. Eng.: A* **2019**, *748*, 205.
[43] Z. Lv, P. Cai, T. Yu, Y. Jin, H. Zhang, W. Fu, T. Zhai, *J. Alloys Compd.* **2017**, *691*, 103.
[44] R. Petráš, V. Škorík, J. Polák, *SSP* **2016**, *258*, 273.
[45] J.-M. Kim, S.-J. Kim, J.-H. Kang, *Mater. Sci. Eng.: A* **2022**, *836*, 142730.
[46] A. Issariyapat, P. Visuttipitukul, T. Song, A. Bahador, J. Umeda, M. Qian, K. Kondoh, *Mater. Charact.* **2020**, *170*, 110700.
[47] H. Berns, W. Theisen, *Ferrous Materials: Steel and Cast Iron*, Springer Science & Business Media **2008**.
[48] A. Lüddecke, N. Hantke, H. Zetzener, J. T. Sehrt, A. Kwade, *Adv. Eng. Mater.* **2025**.
[49] N. Hantke, T. R. Brocksieper, A. Lüddecke, T. Grimm, A. Kwade, J. T. Sehrt, *Adv. Eng. Mater.* **2025**.
[50] A. Bauch, P. Kohlwes, I. Kelbassa, *J. Laser Appl.* **2024**, *36*.
[51] J. Bi, L. Wu, S. Li, Z. Yang, X. Jia, M. D. Starostenkov, G. Dong, *J. Mater. Res. Technol.* **2023**, *26*, 4606.
[52] H. P. Kohl, L. Matthäus, B. Seyfarth, S. Nolte, *Proc. CIRP* **2024**, *124*, 65.